analytical chemistry

pubs.acs.org/ac Article

Enhancing the Sensitivity of the Virus BioResistor by Overoxidation: Detecting IgG Antibodies

Apurva Bhasin,[□] Eric J. Choi,[□] Nicholas P. Drago,[□] Jason E. Garrido, Emily C. Sanders, Jihoon Shin, Ilektra Andoni, Dong-Hwan Kim, Lu Fang, Gregory A. Weiss,* and Reginald M. Penner*

Cite This: *Anal. Chem.* 2021, 93, 11259–11267 Read Online

ACCESS | Metrics & More | Article Recommendations | Supporting Information

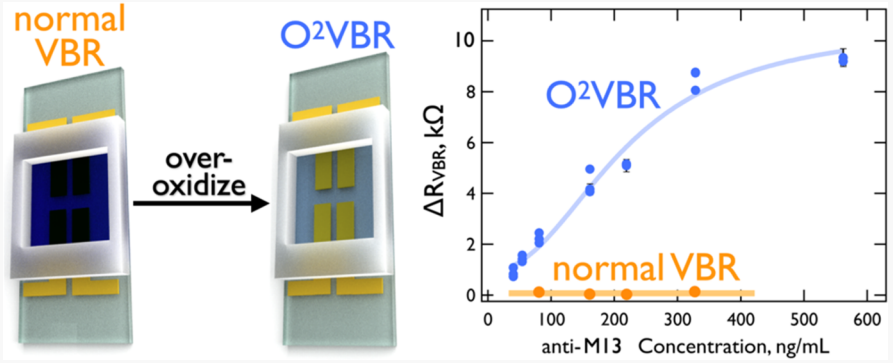

ABSTRACT: The Virus BioResistor (VBR) is a biosensor capable of rapid and sensitive detection of small protein disease markers using a simple dip-and-read modality. For example, the bladder cancer-associated protein DJ-1 (22 kDa) can be detected in human urine within 1.0 min with a limit of detection (LOD) of 10 pM. The VBR uses engineered virus particles as receptors to recognize and selectively bind the protein of interest. These virus particles are entrained in a conductive poly(3,4-ethylenedioxythiophene) or PEDOT channel. The electrical impedance of the channel increases when the target protein is bound by the virus particles. But VBRs exhibit a sensitivity that is inversely related to the molecular weight of the protein target. Thus, large proteins, such as IgG antibodies (150 kDa), can be undetectable even at high concentrations. We demonstrate that the electrochemical overoxidation of the VBR's PEDOT channel increases its electrical impedance, conferring enhanced sensitivity for both small and large proteins. Overoxidation makes possible the detection of two antibodies, undetectable at a normal VBR, with a limit of detection of 40 ng/mL (250 pM), and a dynamic range for quantitation extending to 600 ng/mL.

Biosensors capable of rapid, sensitive quantitation of protein disease markers in a variety of bodily fluids at the point of care could aid in the diagnosis of disease and improve prognoses.[1−3] The Virus BioResistor or VBR is a biosensor that exploits engineered virus particles (Figure S1) as receptors to detect proteins. The device's simple chemiresistor architecture consists of embedded virus particles in a two-layer polymeric channel consisting of a conductive poly(3,4-ethylenedioxythiophene)-poly(styrene sulfonate) or PEDOT-PSS bottom layer prepared by spin coating and an electrodeposited virus-PEDOT top sensing layer.[4−6] We recently demonstrated that VBRs can be used to detect the bladder cancer marker DJ-1 (MW of 22 kDa) with a limit of detection, LOD_{DJ-1}, of 10 pM in human urine.[5,6] However, the VBR is less sensitive to a larger protein, human serum albumin (HSA, 66 kDa), where an LOD_{HSA} of 7.5 nM has been achieved.[5−7] The reduced sensitivity of the VBR can be traced to the reduction of the signal, ΔR_{VBR}, for measurements of HSA compared to DJ-1 (Figure 1). This depressed sensitivity of HSA relative to DJ-1 is observed across the entire VBR dynamic range for the detection of these two proteins.

IgG antibodies (MW of 150 kDa) pose a more challenging problem for the VBR as follows. No signal at all is observed in buffer solutions containing significant concentrations (>300 ng/mL or 1.8 nM) of these large proteins (Figure 1). Together with the data for DJ-1 and HSA, these observations define a trend toward lower VBR sensitivity with increasing protein size. This trend could represent a serious limitation for the practical use of VBRs in point-of-care diagnostics.

Recently,[6] we reported that the sensitivity of VBRs can be enhanced by reducing the thickness of the PEDOT-PSS

Received: May 25, 2021
Accepted: July 21, 2021
Published: August 4, 2021

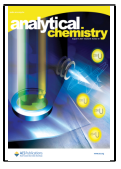

https://doi.org/10.1021/acs.analchem.1c02191
Anal. Chem. 2021, 93, 11259−11267

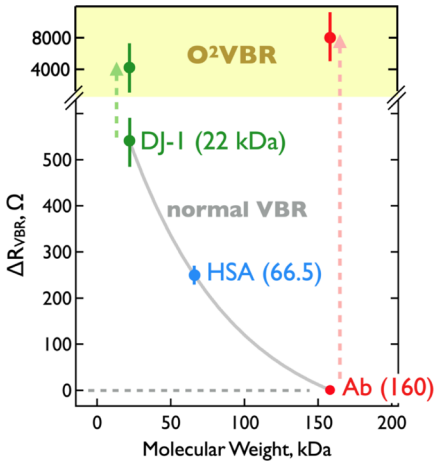

Figure 1. Larger proteins produce less VBR signal. The signal, ΔR_{VBR}, produced by optimized[6] VBRs for three proteins at 100 nM in buffer vs molecular weight of these proteins. The overoxidation process described here produces O²VBRs that generate significantly more signal for both large and small proteins. DJ-1 = protein deglycase,[6] HSA = human serum albumin,[4] Ab = IgG antibody.

bottom layer from 70 (±3 nm) to 48 (±2 nm).[6] This modification enhances the signal amplitude for HSA by a factor of 3−5 across the entire HSA calibration curve.[6] However, this strategy for signal enhancement is limited: 48 nm is the minimum thickness possible for PEDOT-PSS layers prepared by spin coating in our laboratory. It should be noted that all of the "normal" VBR data discussed in this manuscript pertain to the use of VBRs prepared using such ultrathin, 48 nm (±2 nm), PEDOT-PSS layers.[6] The extra sensitivity conferred by this modification is not sufficient to enable the detection of antibodies by VBRs.

A second method for increasing signal amplitudes is described here. It is demonstrated that the electrochemical processing of the VBR channel can significantly increase the signal amplitudes produced by VBRs—beyond the enhancement provided by ultrathin PEDOT-PSS layers—for both small and large proteins. In this electrochemical process, the VBR channel is subjected to irreversible electrochemical oxidation, or "overoxidation",[8−12] resulting in an "O²VBR". Here, the efficacy of overoxidation for "amplifying" signals to measure the concentrations of DJ-1 and two different IgG antibodies is reported. O²VBRs enable the detection of one of the antibodies investigated here at concentrations as low as 40 ng/mL (250 pM), with a dynamic range for quantitation extending to concentrations an order of magnitude higher. Sensor-to-sensor reproducibility is not degraded by overoxidation, and coefficients of variation (CoVs) remain <20% across the entire calibration curve. A mechanism by which overoxidation generates larger VBR signals is also proposed.

EXPERIMENTAL SECTION

Materials and Methods. All materials used were the same as previously reported.[6] Phosphate-buffered saline (PBS, 10× concentration, Sigma-Aldrich) diluted to 1× PBS yielded a phosphate-buffered saline solution at pH 7.4 with a sodium chloride concentration of 0.154 M and a phosphate buffer concentration of 0.01 M. Data for two IgG antibodies are reported: The monoclonal anti-FLAG M2 antibody produced in mouse was purchased from Sigma-Aldrich, and the monoclonal anti-M13 P8 antibody produced in mouse was purchased from Creative Diagnostics. The concentrations of the as-received antibody solutions were determined by performing Bradford assays.

O²VBR Fabrication. The fabrication of O²VBRs follows the same procedure used for the fabrication of VBRs (Figure S3),[4,6] except for the addition of the electrochemical overoxidation process. In summary, bare gold electrodes were O_2 plasma cleaned for 10 min. Well-mixed PEDOT-PSS containing ∼1.5% (v/v) ethylene glycol (EG) was spin-coated onto the electrodes at 2500 rpm for 80 s and baked at 90 °C for 1 h to achieve films with a DC resistance between 260 and 360 Ω. A poly(methylmethacrylate) (PMMA) cell to contain the sample was glued to the PEDOT-PSS thin film, and the device was incubated for 30 min in 1× PBS. The PBS was removed, and a solution of 2.5 mM EDOT, 12.5 mM $LiClO_4$, and 8 nM phage was introduced to the cell. Two voltammetric scans from +0.2 to +0.8 V (vs a mercurous sulfate reference electrode, MSE) at 20 mV/s electropolymerized the EDOT, simultaneously entrapping the phage particles in the PEDOT polymer.[13,14] The overoxidation of the VBR channel was accomplished potentiostatically at +0.8 V vs MSE for 100−150 s in aqueous 12.5 mM $LiClO_4$. This process caused an increase in the DC channel resistance, measured in PBS, from an initial range of 1−2 kΩ before overoxidation to 12−25 kΩ after overoxidation.

Impedance Spectroscopy (IS). VBRs and O²VBRs were washed twice with room temperature 1× PBS and equilibrated in PBS for 20 min prior to the acquisition of triplicate IS measurements in 1× PBS. After the baseline was acquired, the sensor was exposed to an antibody or DJ-1 solution in 1× PBS and allowed to equilibrate for 20 min prior to the acquisition of triplicate IS data sets. Importantly, VBRs and O²VBRs were used for the measurement of a single-antibody solution or a single-DJ-1 solution. All IS measurements used an applied voltage amplitude of 10 mV. A total of 50 impedance measurements were made between 1 Hz and 4 kHz for each data set.

Scanning Electron Microscopy (SEM) Experiments. Scanning electron microscopy (SEM) images were obtained using an FEI Magellan 400L XHR FE-SEM. An accelerative voltage of 2 keV was used for uncoated films and 15 keV for samples sputter-coated with 3 nm of iridium.

Liquid Tapping Atomic Force Microscopy (AFM) Experiments. To obtain the topographical information for VBRs in solution, 50 μL of PBS was pipetted onto the PEDOT-virus layer surface. All AFM images in a liquid environment were collected using an MFP-3D (Asylum Research) in liquid AC (tapping) mode in PBS using DNP-S10 silicon nitride tips (maximum tip radius: 40 nm, Bruker).

RESULTS AND DISCUSSION

O²VBR Fabrication and Characterization. VBRs and O²VBRs share the same device architecture consisting of a two-layer polymeric channel that is deposited on top of two gold electrodes spaced by 1.5 mm. The topmost PEDOT polymer layer also contains virus particles that are engineered using the technique of phage display to recognize and bind a particular protein.[5−7] The gold electrodes measure the electrical impedance of the polymeric channel, which increases when the embedded virus particles bind to their target protein.

A mechanism for signal transduction in the VBR has recently been proposed.[6] Briefly, this mechanism is similar to that proposed for chemiresistive gas sensors that exploit a

https://doi.org/10.1021/acs.analchem.1c02191
Anal. Chem. 2021, 93, 11259−11267

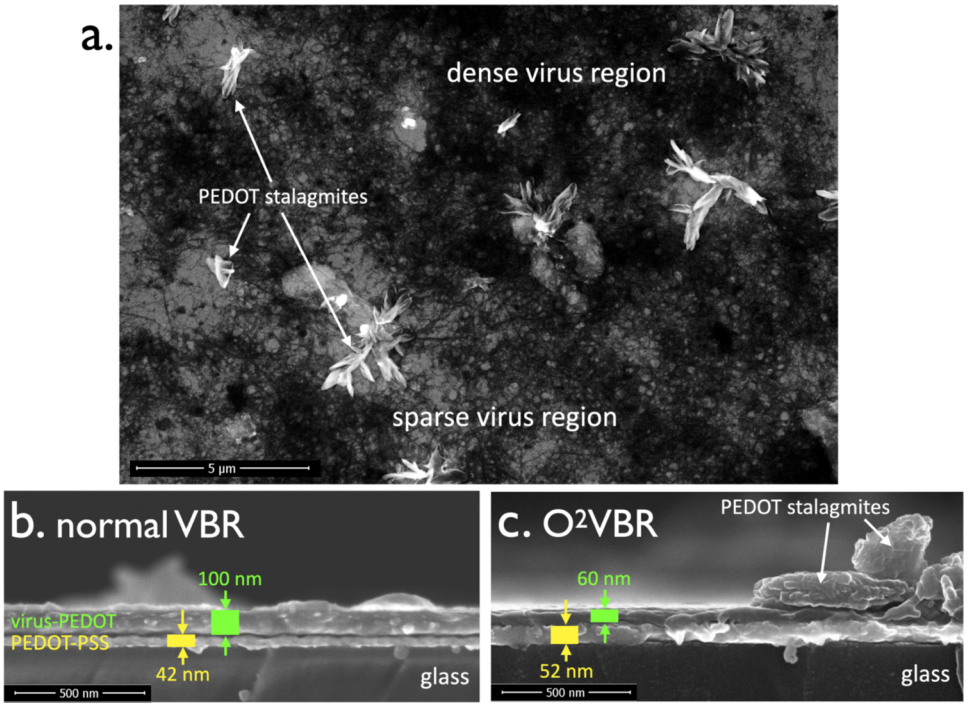

Figure 2. Plan-view SEM image of an O^2VBR channel (a). Darker regions of this image denote regions of high M13 virus density within the virus-PEDOT. Light regions have lower M13 densities. Crystalline PEDOT asperities or "stalagmites" are unrelated to the presence or absence of virus particles. Plan-view images of VBR and O^2VBR are indistinguishable. Cross-sectional view of a VBR (b) and O^2VBR (c) showing thinning of the virus-PEDOT layer from ≈100 to ≈60 nm associated with overoxidation.

conductive carbon/insulating polymer composite chemiresistor.[15−20] In these systems, the chemiresistor is permeated by a vapor-phase molecule with affinity to the polymeric component causing swelling of this channel and a decrease in the volume fraction of the conducting carbon phase, leading to a reduction in the conductivity of the composite. It has been proposed[6] that the virus-PEDOT layer of the VBR operates analogously to these chemiresistors with the conductive PEDOT component of the virus-PEDOT layer undergoing a decrease in volume fraction upon affinity-driven absorption of target protein molecules by the entrained virus particles and concomitant swelling of the virus-PEDOT layer.[6] The resulting increase in the electrical impedance of the VBR is correlated with the concentration of the target protein over a concentration range spanning 2−4 orders of magnitude.[5−7]

The fabrication of an O^2VBRs begins with the fabrication of a VBR—just the final fabrication process step differentiates these two devices. Briefly, starting with patterned gold electrodes on glass (Figure S3a), VBRs are prepared in three steps. First, a PEDOT-PSS layer is deposited by spin coating and dried (Figure S3a, step 1). Second, a poly(methylmethacrylate) or PMMA solution cell with adhesive backing is pressed onto the PEDOT-PSS layer (Figure S3a, step 2). Third, this solution cell is used to contain an aqueous plating solution containing both EDOT and virus particles. From this solution, a virus-PEDOT composite layer is electrodeposited by potentiodynamic oxidation of the EDOT monomer (Figure S3c) for two voltammetric scans to a positive limit of +0.80 V vs MSE causing the formation of insoluble, cationic PEDOT that precipitates on the PEDOT-PSS electrode as a film. Negatively charged virus particles present in the plating solution also deposit with the PEDOT,[14] forming a virus-PEDOT composite top layer (Figure S3a, step 3). As seen in the photograph of a VBR shown in Figure S3b, the resulting VBR "channel" is blue in color and transparent. The blue color is characteristic of the PEDOT-PSS base layer in its oxidized, electronically conductive state.[21,22]

An O^2VBR is obtained by the potentiostatic electrochemical overoxidation of the VBR channel. This is accomplished by stepping the potential of the channel to +0.80 V in aqueous $LiClO_4$ using external reference and counter electrodes (Figure S3a, step 4, and Figure S3d). The overoxidation process causes a bleaching of the blue VBR channel (Figure S3b), rendering the channel of the O^2VBR colorless and transparent, consistent with strong de-doping of the PEDOT-PSS layer of the channel.[23] Nyquist plots for a VBR and O^2VBRs (Figure S3e) show a characteristic semicircular response expected for the VBR.[4−6] The resistive component of the channel impedance, Z_{re}, is approximately equal to the low-frequency limit of these traces, which increases from 2 kΩ for the VBR (green) to 7.5 kΩ for the O^2VBR prepared using a 50 s (red) overoxidation duration and to 16.3 kΩ for the O^2VBR prepared using a 100 s duration of overoxidation (purple). This impedance increase is also consistent with a loss of mobile polaron and bipolaron charge carriers from the VBR channel.[23] The O^2VBRs prepared for this study employed an overoxidation time of 100−150 s within this range produced identical results within our experimental error.

The application of chemical and electrochemical overoxidation to PEDOT for purposes of modifying the electrical conductivity of PEDOT films for applications unrelated to the modification of biosensors has been previously reported.[24−26] Overoxidation is simply the irreversible oxidation of the PEDOT culminating in a sharp reduction in its conductivity. The mechanism of the overoxidation process is proposed[25] to involve a multistep oxidation starting with conversion of the

https://doi.org/10.1021/acs.analchem.1c02191
Anal. Chem. 2021, 93, 11259−11267

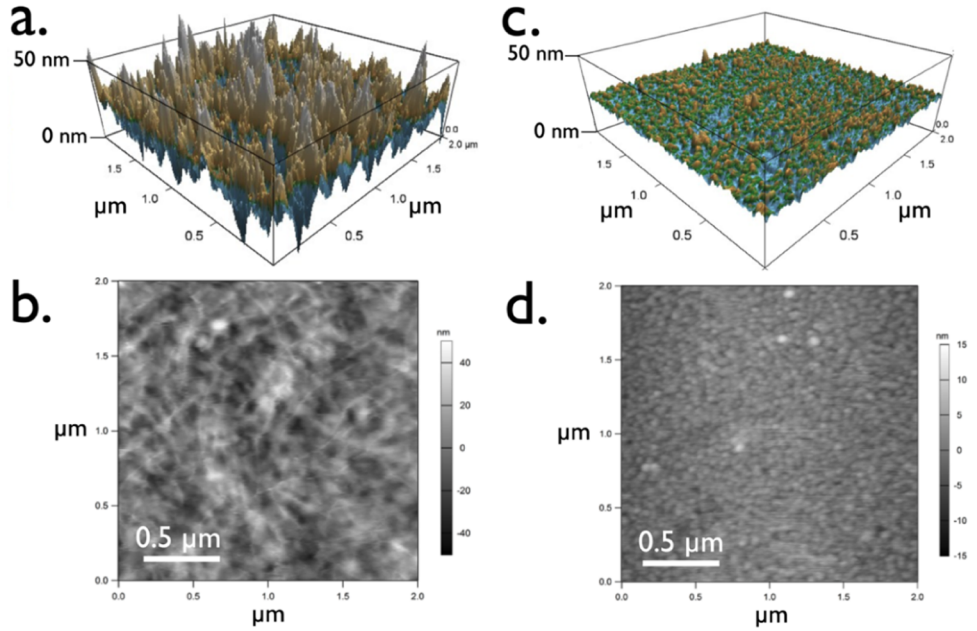

Figure 3. AFM images of VBR (a, b) and O²VBR (c, d) surfaces.

thiophene ring sulfur to a sulfonyl (−S═O) and the elimination of −S═O from the polymer backbone as sulfate, leaving hydroxyl groups in the backbone at both positions adjacent to where the sulfur was formerly located in the thiophene.[25]

Overoxidation alters the topography and thickness of the virus-PEDOT layer exposed at the surface of the VBR channel. Plan-view SEM images of VBRs and O²VBRs (shown in Figure 2a) are indistinguishable, however.[4−6] In these images, M13 virus particles and aggregates of particles appear black because they are electrical insulators and PEDOT, a conductor, appears gray. Regions of high M13 density and low M13 density are thus readily identified. Cross-sectional SEM images (Figure 2b,c) can be used to directly measure the thickness of the virus-PEDOT and PEDOT-PSS layers of the channel. These images show that the PEDOT-PSS bottom layer is consistently 40−55 nm in thickness and unaffected by overoxidation. The virus-PEDOT top layer, however, is reduced in thickness from ≈100 nm in VBRs to ≈60 nm in O²VBRs. In principle, this reduction in thickness of the virus-PEDOT top layer should increase its resistance, contributing to the observed increase in the O²VBR's channel (Figure S3e).

The topography of the virus-PEDOT top layer can be inspected using atomic force microscopy (AFM, Figure 3). These AFM images show a dramatic reduction in surface roughness for O²VBRs relative to VBRs. The filamentous texture seen in AFM images of a VBR is caused by M13 virus particles projecting from the virus-PEDOT surface (Figure 3a,c). This texture is not observed for O²VBR channels (Figure 3b,d), and the surface roughness of the virus-PEDOT layer is reduced, shaving ≈30 nm from the surface. This loss in layer thickness is approximately equal to the thickness reduction of the virus-PEDOT layer seen for O²VBRs compared with VBRs (Figure 2b,c). But it should be noted that, as clearly seen in SEM plan-view images (Figure 2a), overoxidation does not remove virus particles from the interior of the virus-PEDOT layer; they are selectively removed from the surface. As will be clear from the data presented below, this apparent loss of virus particles does not impair the sensitivity of the O²VBR. This surprising result suggests that the carpet of virus particles anchored to the PEDOT layer, but not embedded within it, plays no role in VBR signal transduction.

Two other analytical methods—Raman microprobe spectroscopy (Figure S4) and X-ray photoelectron spectroscopy (XPS, Figures S5 and S6)—have been applied to the characterization of the overoxidation process. While subtle differences between VBRs and O²VBR are apparent from these data, the differences do not provide a chemical justification for the enhancement in signal amplitudes for Abs reported here. Instead, the source of these enhanced signal amplitudes appears to derive from the altered electrical properties of the O²VBR's channel.

VBR and O²VBR Measurements of Antibodies. The responses of VBRs and O²VBR were compared for two IgG antibodies (Abs): anti-M13, an Ab that recognizes and binds the P8 coat protein of the M13 virus, and anti-FLAG, an Ab that binds to FLAG epitopes displayed as *C*-terminal fusions to some of the P8 coat proteins on the M13 virus. Two different M13 virus particles are used as receptors for the detection of these Abs (Figure S1). The first of these, KO7, is a wild-type M13 virus with no modifications to its P8 coat peptides (Figure S1a). This virus presents 2700 copies of P8 on its surface that can be recognized by the anti-M13 antibody. The second virus, M13 FLAG, has a FLAG-tag (with the aa sequence DYKDDDDK, where D = aspartic acid, Y = tyrosine, K = lysine) appended to a subset of the P8 proteins. (Figure S1b). VBRs containing the FLAG-tag bind to anti-FLAG Abs. In principle, M13 KO7 possesses 2700 binding sites for anti-M13, whereas M13-FLAG has a smaller number of binding sites, typically <10% of the total number of P8 proteins, although the precise number is unknown.

An enzyme-linked immunosorbent assay (ELISA) can assess the affinity of anti-M13 and anti-FLAG for the two viruses (Figure S2a,b). Plots of absorbance for the indicator substrate 3,3′,5,5′-tetramethylbenzidine (TNB) as a function of Ab concentration, representing the ELISA signal, show the sigmoidal response expected for Ab binding. The signal at half of the saturation value (EC_{50}) provides an estimate of the

https://doi.org/10.1021/acs.analchem.1c02191
Anal. Chem. 2021, 93, 11259−11267

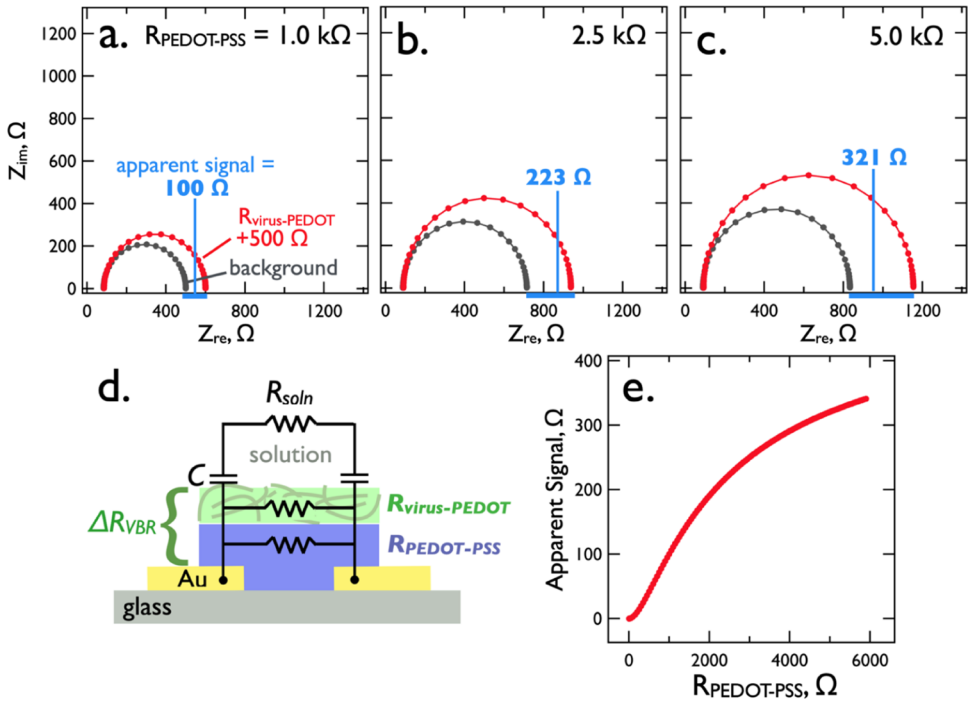

Figure 4. Calculations showing the influence of increased $R_{PEDOT-PSS}$ (as indicated) on the apparent signal, ΔR_{VBR}. (a–c) Calculated Nyquist plots for VBRs as a function of the PEDOT-PSS layer resistance, $R_{PEDOT-PSS}$. In the background traces (black), $R_{virus-PEDOT}$ = 1000 Ω, C_{total} = 10 μF, and R_{soln} = 100 Ω. In red traces, 500 Ω of "signal" are added to $R_{virus-PEDOT}$ for a total of 1500 Ω. The values of other circuit elements remain unchanged. (d) Schematic diagram illustrating the equivalent circuit of the VBR.[4−6] (e) Plot of the apparent signal (ΔR_{VBR}, Ω) vs $R_{PEDOT-PSS}$.

magnitude of the Ab affinity interaction with its virus. The measured values of EC_{50} of 7.3 ng/mL (anti-M13) and 7.6 ng/mL (anti-FLAG) are typical of affinities expected for binding by commercial Abs (Figure S2a,b).

VBRs prepared with either of these two virus receptors, however, do not sense their complementary antibodies, even at Ab concentrations well above EC_{50}. Nyquist plots for two anti-M13 and two anti-FLAG concentrations show no measurable signal, even for Ab concentrations as high as 328 and 556 ng/mL, respectively (Figure S2c–f). The insensitivity of VBRs to Abs is especially surprising because the limit of detection for DJ-1, a much smaller, 22 kDa protein, is just 0.20 ng/mL or 10 pM.[6]

Remediating VBR Ab Insensitivity Using Overoxidation. A remedy for the Ab insensitivity seen for VBRs in Figure S2 can be devised by considering the equivalent circuit responsible for the VBR response (Figure 4d).[4−6] This equivalent circuit has just five elements: two capacitors that provide coupling between the AC voltage signal applied to the channel and the analyte solution, and three resistors, representing the resistances of the analyte solution (R_{soln}), the top virus-PEDOT composite layer ($R_{PEDOT-virus}$), and the bottom PEDOT-PSS layer ($R_{PEDOT-PSS}$). The two capacitors, C, are arranged electrically in series with the electrolyte solution and can be further simplified to a single capacitor, C_{total}, with a value given by $C_{total} = C/2$.

The semicircular Nyquist response produced by VBRs (e.g., Figure S2c–f) results from the parallel arrangement of C_{total} and R_{VBR}, the effective low-frequency resistance of the two-layer polymer channel[6]

$$R_{VBR} \approx \frac{(R_{PEDOT-PSS})(R_{PEDOT-virus})}{R_{PEDOT-PSS} + R_{PEDOT-virus}} \quad (1)$$

In the low-frequency limit (f < 1 Hz), the impedance of C_{total} increases to $Z_{im} = (2\pi f C_{total})^{-1}$, exceeding the value of R_{VBR}. In this low f limit, the coupling of the AC signal into the solution is strongly attenuated and virtually all of the signal is distributed across the current divider $R_{PEDOT-PSS}$ and $R_{virus-PEDOT}$ having an effective resistance, R_{VBR}.

When $R_{PEDOT-PSS}$ and $R_{virus-PEDOT}$ are equal in size, eq 1 predicts that they contribute equally to R_{VBR}, but just the virus-PEDOT layer generates signal related to the presence of a target protein in the solution. This means that just $R_{virus-PEDOT}$, not $R_{PEDOT-PSS}$, is increased by target binding. Unfortunately, $R_{virus-PEDOT}$ cannot be independently measured because it is connected in parallel with $R_{PEDOT-PSS}$. Instead, the VBR signal, given by: $\Delta R_{VBR} = R_{VBR-target} - R_{VBR-cntrl.}$, representing the difference in R_{VBR} in the presence and absence of target protein, is attenuated by the shunting of some current through the PEDOT-PSS bottom layer. To increase ΔR_{VBR}, $R_{PEDOT-PSS}$ must be increased relative to $R_{virus-PEDOT}$. Of course, complete removal of the PEDOT-PSS bottom layer would provide an even more effective solution to this problem; however, this layer is required to serve as an electrode for the deposition of the virus-PEDOT composite top layer (Figure S3c).

Since the response of a VBR can be calculated,[4−6] the influence of changes in $R_{PEDOT-PSS}$ for constant values of a 500 Ω test signal and $R_{virus-PEDOT}$ = 1000 Ω + 500 Ω signal = 1500 Ω can be assessed (Figure 4). When $R_{PEDOT-PSS}$ = 1000 Ω, the apparent signal, ΔR_{VBR}, is just 100 Ω (Figure 4a). For $R_{PEDOT-PSS}$ = 2500 Ω, ΔR_{VBR} increases to 223 Ω (Figure 4b) and $R_{PEDOT-PSS}$ = 5000 Ω produces ΔR_{VBR} = 321 Ω (Figure 4c). Note that both the control trace (black) and the target trace (red) are influenced by $R_{PEDOT-PSS}$. As $R_{PEDOT-PSS}$ increases further (Figure 4e), ΔR_{VBR} asymptotically approaches the true value of the signal, 500 Ω. Our hypothesis is that a disproportionate increase in $R_{PEDOT-PSS}$ vs $R_{virus-PEDOT}$ is also

https://doi.org/10.1021/acs.analchem.1c02191
Anal. Chem. 2021, 93, 11259−11267

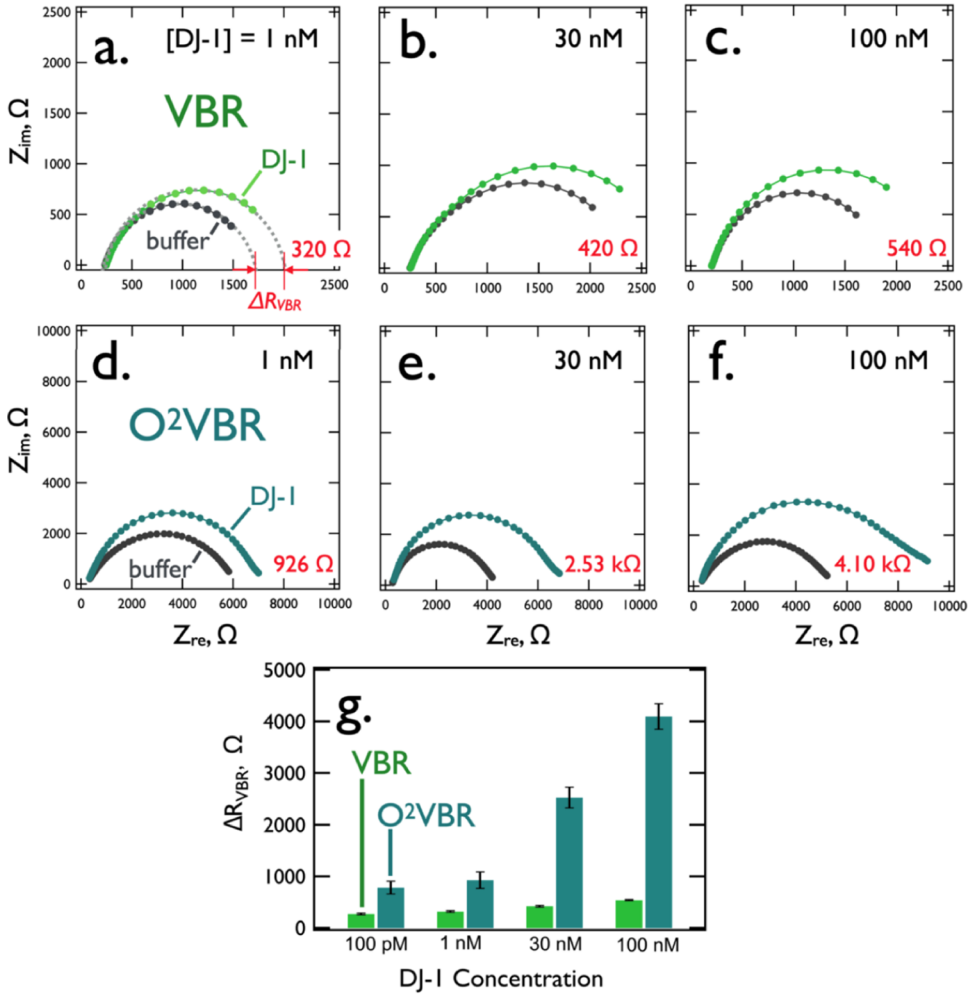

Figure 5. VBR (a–c) and O²VBR (d–f) Nyquist diagrams showing responses to DJ-1 at the specified concentrations. (g) Bar graph of VBR and O²VBR signal amplitudes as a function of DJ-1 concentration. A 3- to 4-fold increase in signal amplitude is observed for the O²VBR across the DJ-1 concentration range from 1 to 100 nM.

occurring during the overoxidation process to produce the O²VBR. Unfortunately, direct confirmation of this mechanism, involving the measurement of resistance for each of these two layers, is not possible because of the nanometer-scale dimensions of both of these layers.

Testing an O²VBR for the Detection of DJ-1. What effect does the overoxidation process have on the detection of DJ-1, a relatively small protein? DJ-1 can be detected at concentrations down to an $LOD_{DJ\text{-}1}$ of 10 pM using a VBR.[6] Nyquist plots for three DJ-1 concentrations (Figure 5a–c) compare three VBRs and three O²VBRs. At concentrations of 1.0, 30, and 100 nM, VBRs generate ΔR_{VBR} signal of 320, 420, and 540 Ω, respectively. For O²VBRs, these signals are increased to 926 Ω, 2.53 kΩ, and 4.10 kΩ—corresponding to factors of 2.9× to 7.6× relative to the VBRs. For [DJ-1] = 100 pM (Nyquist not shown), ΔR_{VBR} increases from 122 Ω (VBR) to 785 Ω (O²VBR), an increase by a factor of 6.4×. The increase in sensitivity provided by the O²VBR for DJ-1 can be seen in the bar graph of Figure 5g.

It should be noted that the Nyquist plots produced by O²VBRs for DJ-1 exhibit a "tail" at low frequencies, deviating from the precise semicircular traces seen in Figure 8a–c, and previously. These deviations correspond to higher values of Z_{im} and Z_{re} at frequencies, f < 10 Hz. These deviations are more pronounced as the concentrations of DJ-1 increase and are nearly absent for control curves acquired in the absence of DJ-1 (Figure 5d,e). This tail is a feature of O²VBRs generally. For the purposes of applying the equivalent circuit of Figure 4d and measuring ΔR_{VBR}, the impedance data set was truncated at 8 Hz prior to curve fitting. This procedure was used to estimate the ΔR_{VBR} signal amplitudes quoted above and also for Ab data discussed below. The mechanistic origin of this deviation is interesting and remains under investigation.

Detecting Antibodies Using O²VBRs. As already noted in Figure S2, in contrast to DJ-1, Abs are not detected by VBRs. For this reason, the Nyquist plots of Figure S2a–d, showing raw impedance data for the detection of two antibodies using four O²VBRs, are striking. ΔR_{VBR} signal amplitudes for these two Abs range from 1 to 8 kΩ range in these examples. The lowest Ab concentration of 81 ng/mL corresponds to 0.54 nM.

The signal-to-noise ratio of the O²VBR measurement (Figure 6e,f) is optimized in the Z_{re} channel at low frequencies ranging from 25 to 60 (Figure 6e, top). At a high frequency, the ordering of concentrations is actually inverted (Figure 6e, bottom). The signal-to-noise ratio of Z_{im} is somewhat lower than Z_{re}, ranging from 7 to 40 for anti-FLAG at 283 and 566 ng/mL.

https://doi.org/10.1021/acs.analchem.1c02191
Anal. Chem. 2021, 93, 11259–11267

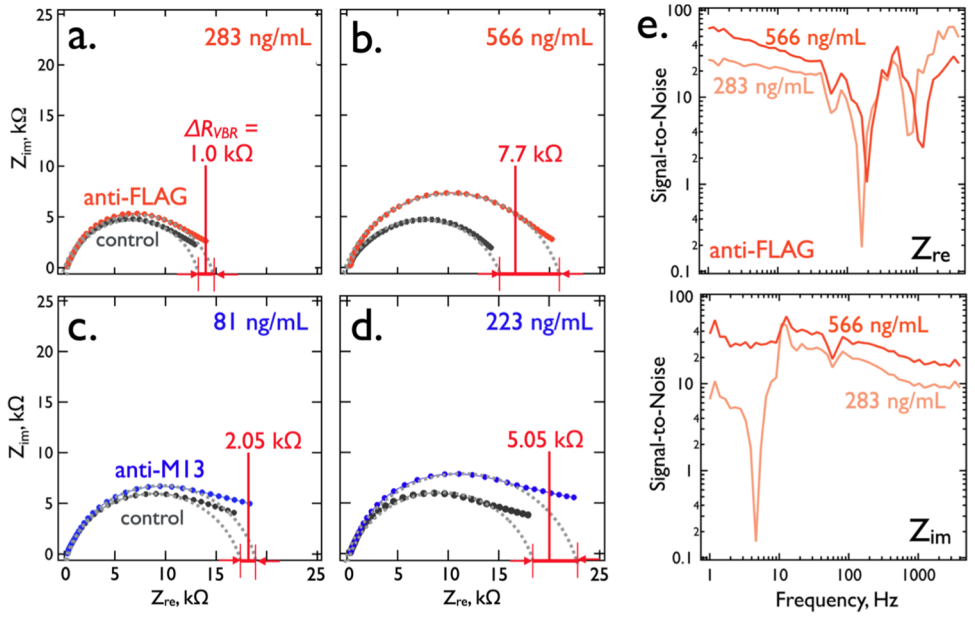

Figure 6. Nyquist diagrams showing responses of four O²VBRs to two antibodies at the specified concentrations. (a–d) Impedance data sets were truncated at 5 Hz. (e) Signal-to-noise (S/N) ratios for the real (Z_{re}) and imaginary (Z_{im}) components of the impedance calculated for the detection of anti-FLAG at the two concentrations. On average, somewhat higher S/N ratios are obtained at a low frequency.

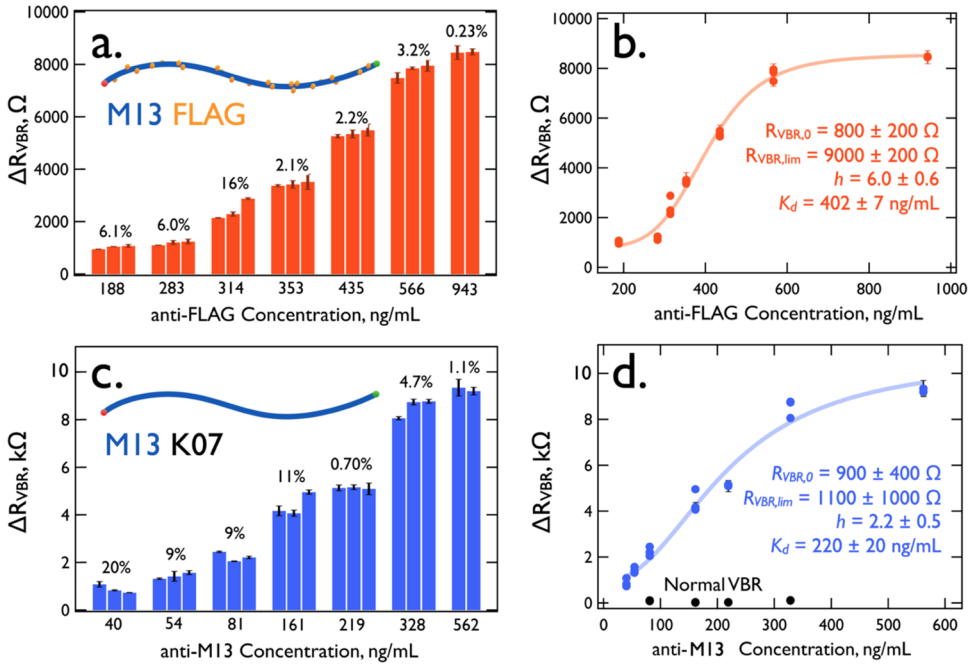

Figure 7. Calibration plots for the detection by O²VBRs of anti-FLAG (a, b) and anti-M13 (c, d). Each bar shown in (a) and (c) correspond to a measurement by a single O²VBR. The coefficient of variation is shown for each concentration. Maximum signal amplitudes for these two antibodies of ≈8 kΩ are similar.

Bar graphs showing the signal produced by each O²VBR and the sensor-to-sensor reproducibility (Figure 7a,c) reveal that low coefficient-of-variation values in the range of 0.2% (highest Ab concentrations) to 20% (lowest concentrations) are obtained. This level of sensor-to-sensor reproducibility is unusual and testifies to the reproducibility of the overoxidation process.

Calibration curves for both Abs show classical sigmoidal behavior that conforms to the Hill equation (Figure 7b,d)[27]

$$\Delta R_{VBR} = \Delta R_{VBR,0} + \frac{\Delta R_{VBR,lim} - \Delta R_{VBR,0}}{1 + \left(\frac{K_D}{[Ab]}\right)^h} \quad (2)$$

Fitting the calibration data using eq 2 with fitting parameters h and K_D provides values of 2.2 ± 0.5 (anti-M13) and 6.0 ± 0.6 (anti-FLAG). Values of h greater than 1.0 are indicative of strong positive cooperativity, meaning that the microscopic dissociation constant, K_D, is decreased (the affinity interaction is increased) as the fraction of binding sites occupied by the target protein increases.[27] This has the effect of compressing

https://doi.org/10.1021/acs.analchem.1c02191
Anal. Chem. 2021, 93, 11259–11267

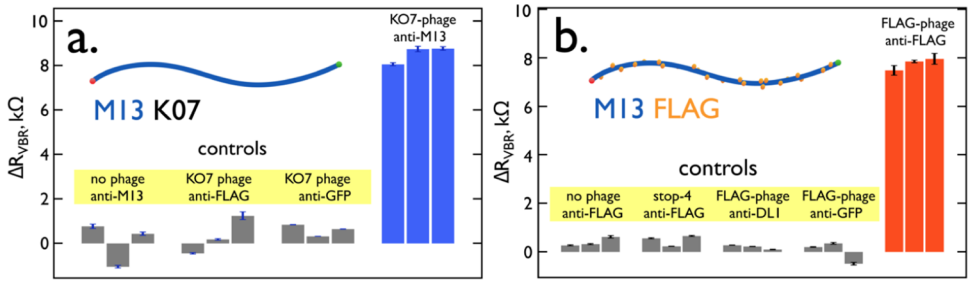

Figure 8. Control experiments for the detection by O²VBRs of anti-M13 and anti-FLAG. All experiments were performed using 100 nM target (anti-DL-1, anti-GFP, anti-FLAG, and anti-M13) in PBS.

the binding curve resulting in a narrow range of Ab concentrations over which the O²VBR is responsive. This resulting dynamic range is 200−600 ng/mL for anti-FLAG (h = 6.0) and 50−500 ng/mL for anti-M13 (h = 2.2). K_D values of 220 (±20) ng/mL (anti-M13) and 402 (±7) ng/mL (anti-FLAG) are observed for these two Abs.

Finally, the issue of selectivity of the O²VBR response is addressed by the control experiments summarized in Figure 8. Shown in these controls are no phage controls, in which no phage is present in the electrodeposited PEDOT top layer. Two other antibodies, anti-DL-1 (DL-1 is a phage displaying peptide epitopes for DJ-1) and anti-GFP (green fluorescent protein), were also assessed. And O²VBRs containing M13 phage were assessed as controls for the detection of anti-FLAG (Figure 8). The level of selectivity seen here is similar to that reported for VBRs in our prior studies.[5−7]

SUMMARY

The sensitivity of Virus BioResistors (VBRs) is dramatically enhanced by applying a simple electrochemical process in which the conductivity of the polymeric channel is reduced by a potentiostatic overoxidation process requiring just 3−5 min. The resulting biosensors are termed O²VBRs. For a smaller protein, DJ-1 (22 kDa) at 100 nM, the signal amplitude generated by O²VBRs increases by a factor of 3−7×, relative to unmodified VBRs. For much larger IgG antibodies (150 kDa) that are undetectable by VBRs at 100 nM, a signal of 8 kΩ is obtained using O²VBRs at 100 nM.

The data coupled with our calculations implicate a mechanism for the increased sensitivity of O²VBRs that involves the strong and disproportionate increase in resistance of the PEDOT-PSS base layer of the channel relative to the virus-PEDOT sensing layer. However, this study does not rule out the influence on sensitivity of significant morphological changes caused by the oxidation process that may, for example, increase the porosity or mean pore diameter of the virus-PEDOT layer. Pronounced changes to the topography of the virus-PEDOT layer caused by overoxidation are observed in SEM and AFM images, but we are not able to determine their influence, if any, on the ability of large proteins to permeate the virus-PEDOT layer.

ASSOCIATED CONTENT

Supporting Information

The Supporting Information is available free of charge at https://pubs.acs.org/doi/10.1021/acs.analchem.1c02191.

Two virus receptors used in this study; demonstration of VBR insensitivity to two antibodies; additional experimental details; Raman spectroscopy; and X-ray photoelectron spectroscopy (PDF)

AUTHOR INFORMATION

Corresponding Authors

Gregory A. Weiss − *Department of Chemistry, University of California, Irvine, Irvine, California 92697, United States; Department of Pharmaceutical Sciences and Department of Molecular Biology & Biochemistry, University of California, Irvine, Irvine, California 92697, United States;* orcid.org/0000-0003-0296-9846; Email: gweiss@uci.edu

Reginald M. Penner − *Department of Chemistry, University of California, Irvine, Irvine, California 92697, United States;* orcid.org/0000-0003-2831-3028; Email: rmpenner@uci.edu

Authors

Apurva Bhasin − *Department of Chemistry, University of California, Irvine, Irvine, California 92697, United States*

Eric J. Choi − *Department of Chemistry, University of California, Irvine, Irvine, California 92697, United States;* orcid.org/0000-0003-3287-1284

Nicholas P. Drago − *Department of Chemistry, University of California, Irvine, Irvine, California 92697, United States;* orcid.org/0000-0002-3790-552X

Jason E. Garrido − *Department of Chemistry, University of California, Irvine, Irvine, California 92697, United States*

Emily C. Sanders − *Department of Chemistry, University of California, Irvine, Irvine, California 92697, United States;* orcid.org/0000-0003-1043-5772

Jihoon Shin − *School of Chemical Engineering, Sungkyunkwan University, Suwon, Gyeonggi-do 16419, South Korea*

Ilektra Andoni − *Department of Chemistry, University of California, Irvine, Irvine, California 92697, United States*

Dong-Hwan Kim − *School of Chemical Engineering, Sungkyunkwan University, Suwon, Gyeonggi-do 16419, South Korea;* orcid.org/0000-0002-2753-0955

Lu Fang − *Department of Automation, Hangzhou Dianzi University, Hangzhou 310018, China*

Complete contact information is available at: https://pubs.acs.org/10.1021/acs.analchem.1c02191

Author Contributions

□A.B., E.J.C., and N.P.D. contributed equally to this work.

Notes

The authors declare the following competing financial interest(s): R.M.P., G.A.W., and A.B. have a financial interest in a company, PhageTech, Inc., that is commercializing the technologies described here. The terms of this arrangement

https://doi.org/10.1021/acs.analchem.1c02191
Anal. Chem. 2021, 93, 11259−11267

have been reviewed and approved by the University of California, Irvine, in accordance with its conflict-of-interest policies.

■ ACKNOWLEDGMENTS

R.M.P. acknowledges the financial support of this work by the National Science Foundation, through contract CBET-1803314. R.M.P. and G.A.W. acknowledge support from the National Cancer Institute of the NIH (1R33CA206955-01), PhageTech, Inc. (PHAGE-203015), and the Chao Family Comprehensive Cancer Center, UC, Irvine. FE-SEM data were acquired using the instrumentation of the LEXI (lexi.eng.uci.edu/) and IMRI (ps.uci.edu/imri/) facilities at UCI. Raman microprobe spectra were collected in the UCI Laser Spectroscopy Laboratory (https://www.chem.uci.edu/dmitryf/index.html). X-ray photoelectron spectra were obtained in the UCI Surface Science Facility (https://ccam.uci.edu/facilities/ssf/). This research was also supported by the MOTIE (Ministry of Trade, Industry, and Energy) in Korea, under the Fostering Global Talents for Innovative Growth Program (P0008746) supervised by the Korea Institute for Advancement of Technology (KIAT).

■ REFERENCES

(1) Cheng, C.-M.; Kuan, C.-M.; Chen, C.-F. *In-Vitro Diagnostic Devices*; Springer International Publishing: Cham, 2016.
(2) McDonnell, B.; Hearty, S.; Leonard, P.; O'Kennedy, R. *Clin. Biochem.* **2009**, *42*, 549−561.
(3) Gubala, V.; Harris, L. F.; Ricco, A. J.; Tan, M. X.; Williams, D. E. *Anal. Chem.* **2012**, *84*, 487−515.
(4) Bhasin, A.; Ogata, A. F.; Briggs, J. S.; Tam, P. Y.; Tan, M. X.; Weiss, G. A.; Penner, R. M. *Nano Lett.* **2018**, *18*, 3623−3629.
(5) Bhasin, A.; Drago, N. P.; Majumdar, S.; Sanders, E. C.; Weiss, G. A.; Penner, R. M. *Acc. Chem. Res.* **2020**, *53*, 2384−2394.
(6) Bhasin, A.; Sanders, E. C.; Ziegler, J. M.; Briggs, J. S.; Drago, N. P.; Attar, A. M.; Santos, A. M.; True, M. Y.; Ogata, A. F.; Yoon, D. V.; et al. *Anal. Chem.* **2020**, *92*, 6654−6666.
(7) Bhasin, A.; Ogata, A. F.; Briggs, J. S.; Tam, P. Y.; Tan, M. X.; Weiss, G. A.; Penner, R. M. *Nano Lett.* **2018**, *18*, 3623−3629.
(8) Fan, J.; Rezaie, S. S.; Facchini-Rakovich, M.; Gudi, D.; Montemagno, C.; Gupta, M. *Org. Electron.* **2019**, *66*, 148−155.
(9) Drillet, J.-F.; Dittmeyer, R.; Jüttner, K. *J. Appl. Electrochem.* **2007**, *37*, 1219−1226.
(10) Özcan, A.; İlkbaş, S. *Anal. Chim. Acta* **2015**, *891*, 312−320.
(11) Gorduk, O. *Anal. Lett.* **2020**, *53*, 1034−1052.
(12) Tehrani, P.; Kanciurzewska, A.; Crispin, X.; Robinson, N.; Fahlman, M.; Berggren, M. *Solid State Ionics* **2007**, *177*, 3521−3527.
(13) Donavan, K. C.; Arter, J. A.; Pilolli, R.; Cioffi, N.; Weiss, G. A.; Penner, R. M. *Anal. Chem.* **2011**, *83*, 2420−2424.
(14) Donavan, K. C.; Arter, J. A.; Weiss, G. A.; Penner, R. M. *Langmuir* **2012**, *28*, 12581−12587.
(15) Field, C. R.; Yeom, J.; Salehi-Khojin, A.; Masel, R. I. *Sens. Actuators, B* **2010**, *148*, 315−322.
(16) Alizadeh, T.; Rezaloo, F. *Sens. Actuators, B* **2013**, *176*, 28−37.
(17) Llobet, E. *Sens. Actuators, B* **2013**, *179*, 32−45.
(18) Hangarter, C. M.; Chartuprayoon, N.; Hernández, S. C.; Choa, Y.; Myung, N. V. *Nano Today* **2013**, *8*, 39−55.
(19) Doleman, B. J.; Sanner, R. D.; Severin, E. J.; Grubbs, R. H.; Lewis, N. S. *Anal. Chem.* **1998**, *70*, 2560−2564.
(20) Karr, L. J.; Shafer, S. G.; Harris, J. M.; Van Alstine, J. M.; Snyder, R. S. *J. Chromatogr. A* **1986**, *354*, 269−282.
(21) Kawahara, J.; Ersman, P. A.; Engquist, I.; Berggren, M. *Org. Electron.* **2012**, *13*, 469−474.
(22) DeLongchamp, D.; Hammond, P. T. *Adv. Mater.* **2001**, *13*, 1455−1459.
(23) Zozoulenko, I.; Singh, A.; Singh, S. K.; Gueskine, V.; Crispin, X.; Berggren, M. *ACS Appl. Polym. Mater.* **2019**, *1*, 83−94.
(24) Tehrani, P.; Kanciurzewska, A.; Crispin, X.; Robinson, N. D.; Fahlman, M.; Berggren, M. *Solid State Ionics* **2007**, *177*, 3521−3527.
(25) Fan, J.; Rezaie, S. S.; Facchini-Rakovich, M.; Gudi, D.; Montemagno, C.; Gupta, M. *Org. Electron.* **2019**, *66*, 148−155.
(26) Zhou, C.; Liu, Z.; Du, X.; Ringer, S. P. *Synth. Met.* **2010**, *160*, 1636−1641.
(27) Kurganov, B.; Lobanov, A.; Borisov, I.; Reshetilov, A. *Anal. Chim. Acta* **2001**, *427*, 11−19.

https://doi.org/10.1021/acs.analchem.1c02191
Anal. Chem. 2021, 93, 11259−11267